Title

The sinoatrial node extracellular matrix promotes pacemaker phenotype and protects automaticity in engineered heart tissues from cyclic strain

Journal

Cell Reports, 42(12)

ISSN

2639-1856

Authors

Sun, Yao-Hui

Kao, Hillary KJ

Thai, Phung N

et al.

Publication Date

2023-12-01

DOI

10.1016/j.celrep.2023.113505

Peer reviewed

HHS Public Access

Author manuscript

Cell Rep. Author manuscript; available in PMC 2024 January 16.

Published in final edited form as:

Cell Rep. 2023 December 26; 42(12): 113505. doi:10.1016/j.celrep.2023.113505.

The sinoatrial node extracellular matrix promotes pacemaker phenotype and protects automaticity in engineered heart tissues from cyclic strain

Yao-Hui Sun[1,2], **Hillary K.J. Kao**[1,2], **Phung N. Thai**[1], **Regan Smithers**[1,2], **Che-Wei Chang**[5], **Dalyir Pretto**[1,2], **Sergey Yechikov**[1,2], **Sarah Oppenheimer**[1,2,3], **Amanda Bedolla**[1,2,3], **Brooke A. Chalker**[1,2,4], **Rana Ghobashy**[1,2,3], **Jan A. Nolta**[2], **James W. Chan**[5], **Nipavan Chiamvimonvat**[1,6], **Deborah K. Lieu**[1,2,7,*]

[1]Department of Internal Medicine, Division of Cardiovascular Medicine, University of California, Davis, Davis, CA 95616, USA

[2]Institute for Regenerative Cures and Stem Cell Program, University of California, Davis, Sacramento, CA 95817, USA

[3]Bridges to Stem Cell Research Program, California State University, Sacramento, Sacramento, CA 95817, USA

[4]Bridges to Stem Cell Research Program, Cal Poly Humboldt, Humboldt, CA 95521, USA

[5]Department of Pathology and Laboratory Medicine, University of California, Davis, Sacramento, CA 95817, USA

[6]Department of Veterans Affairs, Northern California Health Care System, Mather, CA 95655, USA

[7]Lead contact

SUMMARY

The composite material-like extracellular matrix (ECM) in the sinoatrial node (SAN) supports the native pacemaking cardiomyocytes (PCMs). To test the roles of SAN ECM in the PCM phenotype and function, we engineered reconstructed-SAN heart tissues (rSANHTs) by recellularizing porcine SAN ECMs with hiPSC-derived PCMs. The hiPSC-PCMs in rSANHTs self-organized into clusters resembling the native SAN and displayed higher expression of pacemaker-specific genes and a faster automaticity compared with PCMs in reconstructed-left ventricular heart tissues (rLVHTs). To test the protective nature of SAN ECMs under strain, rSANHTs and rLVHTs were

*Correspondence: dklieu@ucdavis.edu.

AUTHOR CONTRIBUTIONS

Conceptualization, methodology, writing—draft, review & editing, visualization: Y.H.S. and D.K.L.; investigation: Y.H.S., H.K.J.K., P.N.T., R.S., C.W.C., D.P., S.Y., S.O., A.B., B.A.C., and R.G.; supervision: J.A.N., J.W.C., N.C., and D.K.L.; funding acquisition: D.K.L.

DECLARATION OF INTERESTS

D.K.L. is a consultant for Novoheart, Ltd.

SUPPLEMENTAL INFORMATION

Supplemental information can be found online at https://doi.org/10.1016/j.celrep.2023.113505.

transplanted onto the murine thoracic diaphragm to undergo constant cyclic strain. All strained-rSANHTs preserved automaticity, whereas 66% of strained-rLVHTs lost their automaticity. In contrast to the strained-rLVHTs, PCMs in strained-rSANHTs maintained high expression of key pacemaker genes (HCN4, TBX3, and TBX18). These findings highlight the promotive and protective roles of the composite SAN ECM and provide valuable insights for pacemaking tissue engineering.

In brief

Sun et al. demonstrate that the sinoatrial node extracellular matrix (SAN ECM) promotes the pacemaker phenotype and safeguards its automaticity under mechanical strain in engineered heart tissues. These findings offer significant insights into the development of bioengineered pacemakers.

Graphical abstract

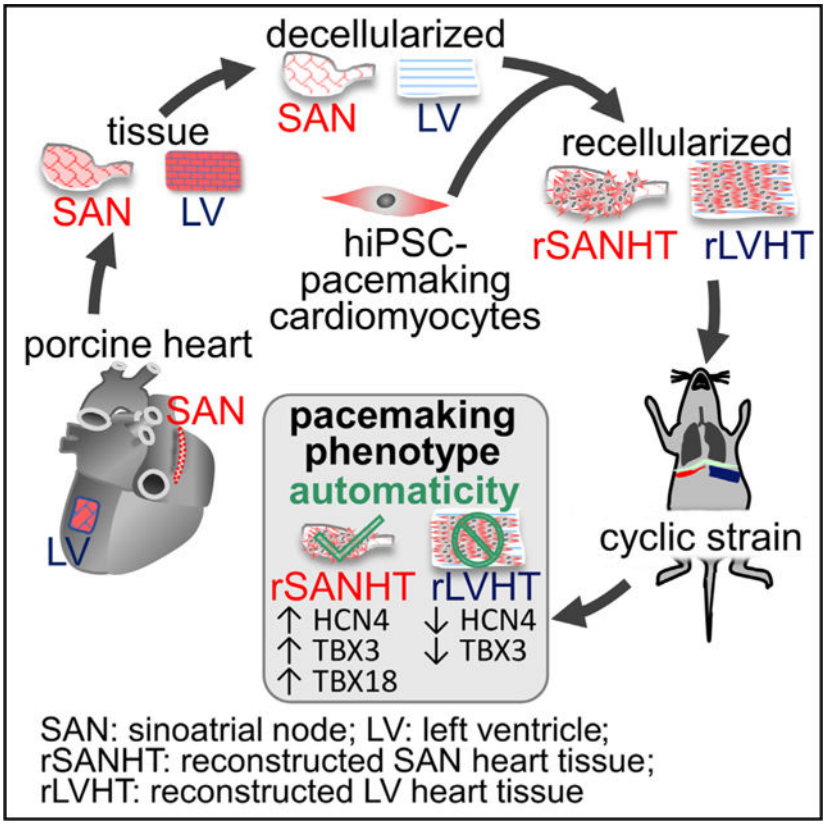

INTRODUCTION

The sinoatrial node (SAN) is the site where the primary cardiac pacemaker is located in the heart.[1] Its limited regenerative capacity poses a significant challenge in treating SAN dysfunction,[2,3] which often requires costly and immediate medical interventions, such as lifelong dependence on implanted electronic pacemakers.[4–6] While electronic pacemakers are effective in restoring the cardiac rhythm and improving patients' quality of life,

they have a number of inevitable drawbacks associated with electronics, such as lack of autonomic responsiveness, risks of infections, limited battery life, and inability to adapt to growth in pediatric patients.[7,8] Human induced pluripotent stem cell (hiPSC)-based biopacemakers offer a promising alternative to the electronic pacemakers.[9]

Generation of human pacemaking cardiomyocytes (PCMs) from hiPSCs has recently been successfully demonstrated.[10–14] Although these electrical impulse-generating cells constitute the functional component of an engineered biopacemaker tissue, the extracellular matrix (ECM) scaffold is an equally important ancillary component that supports and maintains the automaticity in the PCMs. The decellularized ECM derived from a tissue of interest in theory is the most suitable matrix scaffold for engineering that same tissue as it bestows the native microenvironment to the resident cells.[15] It provides not only biochemical cues but also the native tissue architecture and biophysical properties, including mechanical strength and stiffness, to support cell survival, differentiation, and function.[16] The ECM from the left ventricle (LV) has been studied extensively and used in engineering contractile heart tissues with working CMs,[17–24] but the effects of the SAN ECMs on hiPSC-PCMs are unknown. Based on the reported biomechanical properties and biochemical compositions unique to the porcine SAN ECM in comparison with the LV counterpart, we had proposed a composite material model describing how the SAN ECMs may shield the resident PCMs from cyclic mechanical strain and provide critically conducive biochemical and biomechanical signals in protecting and sustaining their pacemaking function.[25]

Taking a stepwise reverse engineering approach to test our proposed model, we engineered reconstructed-SAN heart tissues (rSANHTs) by recellularizing the decellularized porcine SAN ECMs with hiPSC-PCMs. For rigorous experimental design, hiPSC-PCMs were also seeded in porcine LV ECMs to generate reconstructed-LV heart tissues (rLVHTs) as controls. In contrast to the hiPSC-PCMs in rLVHTs, those in the rSANHTs exhibited phenotype and function that resembled the native PCMs. To test the mechanical insulating property of the composite SAN ECM, paired rSANHTs and rLVHTs are subjected to repeated mechanical strain at a novel *in vivo* cardiac-like site—the murine thoracic diaphragm—with human fetal-like heart rate. Strained hiPSC-PCMs in the SAN ECM continued to express high pacemaking genes and automaticity in contrast to those in the LV ECM. Our data demonstrated that the SAN ECMs guided the hiPSC-PCMs to arrange into an SAN-like cellular organization, promoted PCM phenotype and function in these cells, but most importantly protected and sustained the self-organization and pacemaking phenotype of hiPSC-PCMs similar to resident PCMs in the SAN even under cyclic mechanical strain. The findings highlight the importance of incorporating a composite SAN-like ECM in the design of engineered biopacemakers.

RESULTS

Generation of rSANHTs and rLVHTs

To test the effects of ECMs on human PCMs, hiPSC-PCMs were differentiated using our recently published small molecule protocol[11] that temporally inhibited both the canonical Wnt signaling with IWR1 and Nodal signaling with SB431542 (SB) in the

cardiac mesoderm stage from differentiating day 3–5 (Figure 1A), resulting in ~78% CMs identified by the positive expression for cardiac troponin T (cTNT) on day 20 post-differentiation (Figure 1B). While the IWR1+SB-differentiated hiPSC-CMs expressed pacemaking hyperpolarization-activated cyclic nucleotide-modulated (HCN)4 channels (Figure 1C), they were heterogeneous in CM subtypes, including ventricular-, atrial-, and pacemaker-like CMs, as classified by optically recorded action potentials (APs) using voltage-sensitive dye FluoVolt in single cells (Figure 1D). Notably, the yield of the PCM-like fraction from the IWR1+SB-differentiated cultures was 3-fold higher compared with the culture differentiated by an established protocol[26] with IWR1 (26% vs. 8%, $p < 0.01$ by χ^2 test; Figure 1E). Although not all hiPSC-differentiated CMs are classified as the PCM subtype by APs, we had demonstrated by flow cytometry that nearly all IWR1+SB-differentiated CMs are positive for pacemaking genes HCN4, T-box (TBX)3, TBX18, and short stature homeobox (SHOX)2 with ~50%–100% higher expression than the IWR1 protocol.[11] Most importantly, our modified protocol induced hiPSC-CMs with a faster frequency of automaticity in the cultures than the control IWR1 protocol (median: 162 vs. 60 bpm, $p < 0.01$; Figure 1F; Video S1). These IWR1+SB-differentiated hiPSC-PCMs were used to recellularize the decellularized SAN ECMs (Figures S1 and S2) to fabricate the rSANHTs (Figure 2A). The same cells were seeded in the LV ECMs (Figures S1 and S2) to generate the rLVHTs as control for a head-to-head, direct comparison of the ECM effects on hiPSC-PCMs (Figure 2A). Spontaneous contractions in a broad range of frequencies from 6 to 140 bpm were observed in the hiPSC-PCMs within 2–4 days of rHT construction (Videos S2 and S3). Automaticity of engineered tissues could be maintained for >100 days in culture.

rSANHTs structurally resemble the native SAN

Whole-mount rSANHTs and rLVHTs immunostained with a CM marker cTNT 14 days after culture show that hiPSC-PCMs in the rSANHTs have self-organized into densely compact but randomly oriented clusters, whereas those in the rLVHTs are in bundles that aligned along the ECM (Figure 2B). The cellular organization in both rHTs resembled their respective native counterpart. Morphometric analysis of nuclei from high-resolution fluorescence images (Figure S3A) demonstrated that the hiPSC-PCMs in the rSANHT were significantly less elongated compared with those in the rLVHTs (median aspect ratio: 1.51 vs. 1.88, $p < 0.05$), recapitulating the features observed in the native SAN compared with the native LV (median aspect ratio: 1.60 vs. 2.10, $p < 0.01$; Figure 2C) and the native atrial myocardium (median aspect ratio: 2.43, $p < 0.01$ compared with the native SAN; Figure S3C). Although not statistically significant, cells in the SANHT were oriented in a less uniformed direction compared with cells in rLVHTs (median angle: 1.42 vs. 0.93 Rad; Figure 2D), following a similar trend observed between the native SAN and the adjacent atrial myocardium (median angle: 2.04 vs. 0.25 Rad, $p < 0.01$; Figure S3D) or the native SAN relative to the native LV (median angle: 2.04 vs. 0.83 Rad, $p < 0.01$; Figures 2D and S4). Hence, the quantified morphometry suggests that hiPSC-PCMs in the rSANHTs were organized structurally similar to PCMs in the native SAN and distinctly differed from those in the rLVHTs. Of note, the cellular organization on the SAN and LV ECM closely follows the respective ECM scaffold organization revealed by wheat germ agglutinin staining (Figure S5).

The SAN ECM promotes pacemaker gene expression in hiPSC-PCMs

To determine the effects of the SAN ECM on the transcriptional changes in hiPSC-PCMs relative to those in the LV ECMs, we conducted quantitative real-time PCR analysis on whole rHTs for a select group of pro-pacemaking genes after 2 weeks of *in vitro* culture (Figure 3A). Our results showed that transcription factors associated with SAN development, *TBX18* and Islet (*ISL)1*, were 6- and 3-fold higher in the rSANHTs relative to the rLVHT control, respectively. Pacemaker channels, *HCN4* and *HCN1*, were both 2-fold higher in the rSANHTs compared with the rLVHTs, albeit only *ISL1* and *HCN1* ($p < 0.01$ and $p < 0.05$, respectively) reached statistical significance (Figure 3B). The pituitary homeobox (*PITX) 2* and *TBX3* transcription were comparable between the rHTs, but *SHOX2* was marginally increased in the rSANHTs (Figure 3B). Protein expression of select pacemaking genes and ventricular-specific marker were assessed by immunostaining followed by image analysis (Figures 3C and 3D). Immunostaining analysis of $cTNT^{+}$ hiPSC-PCMs revealed stronger protein expression of HCN4 channels, and TBX18 transcription factors in the rSANHTs compared with rLVHT. The TBX3 protein expression was comparable between the two rHTs, consistent with the transcript analysis. Immunofluorescent staining of ventricular-specific myosin light chain (MLC)2v showed a relatively low abundance of the protein in both rHTs. Our findings suggest that utilizing the SAN ECM as a scaffold for the hiPSC-PCMs provides a suitable natural microenvironment for their growth and development, supported by the expression of pacemaking genes.

The SAN ECM promotes functional pacemaking phenotype in hiPSC-PCMs

To evaluate the contractile function of hiPSC-PCMs in the rHTs, we utilized the MUSCLEMOTION algorithm[27] to generate contractile traces and particle imaging velocimetry (PIV)[28,29] to accurately quantify the maximum contractile displacement of hiPSC-PCMs (Figure 4A). At 2 weeks post-construction of rHTs, PIV revealed a maximum displacement of ~2 μm for the CM clusters in the rSANHT and a higher displacement reaching 5 μm in the CM bundles of rLVHT (Figure 4B; Video S4). Additionally, we observed a >3-fold reduction in the mean contraction amplitude in the rSANHTs compared with the rLVHTs (median: 6,761 vs. 35,389 a.u., $p < 0.01$; Figures 4C and 4D). The contractions in the rSANHTs also exhibited a slower kinetics compared with the LV counterpart, as indicated by an increased time-to-peak (median: 504 vs. 151 ms, $p < 0.01$) and relaxation time (median: 431 vs. 302 ms, $p < 0.01$).

To investigate the electrophysiology and automaticity of the hiPSC-CMs in the rHTs, we utilized a genetically engineered hiPSC line that encoded an ultrasensitive calcium indicator, GCaMP6f,[30] which enabled us to monitor intracellular calcium dynamics as a surrogate of AP recording in individual CMs as well as in the engineered heart tissues (Figure 4E). The GCaMP6f-hiPSC line was chosen to avoid possible uneven outside-in loading of calcium probes in the rHTs. We differentiated GCaMP6f-PCMs using the same IWR1+SB protocol and then constructed rSANHTs and rLVHTs. We recorded calcium transients (CaTs) optically (Figure 4F) and observed spontaneous and robust CaTs in both rHTs over the 2 weeks of *in vitro* culture (Videos S5 and S6). CaTs of GCaMP6f-PCMs in the rSANHT compared with those in the rLVHT, exhibited a statistically faster frequency of spontaneous CaTs (median: 52 vs. 35 bpm, $p < 0.01$) that were smaller in amplitude (median $\Delta F/F_0$: 59

vs. 140%, $p < 0.01$; Figure 4G; Table S1; three biological replicates), which are consistent with a PCM-like functional phenotype. Collectively, these functional data on contractions and CaTs suggest a weaker contractile function but more robust automaticity—hallmark features of PCMs—in the hiPSC-PCMs residing in rSANHTs compared with those in the rLVHTs. This is consistent with the notion that the native SAN ECM microenvironment promotes functionally pacemaker-like hiPSC-CMs.

SAN ECM preserves pacemaking phenotype in hiPSC-PCMs subjected to cyclic mechanical strain *in vivo*

Cyclic mechanical stretch is constantly imposed on all CMs in the heart. Naturally, it has been commonly employed as a strategy to enhance the maturation of contractile hiPSC-CMs through the activation of mechanotransduction signaling that can direct the CM phenotype, including cellular hypertrophy and myofilament alignment,[31,32] which are notably counter to the key features of PCMs. In this study, we directly tested the mechanical protective effects of the SAN ECM on the resident PCMs that were proposed in our comprehensive report on the SAN ECM.[25] Paired rSANHTs and rLVHTs were contralaterally transplanted on the thoracic diaphragm of immune-deficient NOD-SCID gamma (NSG) mice and subjected to a cardiac-like microenvironment with cyclic mechanical strain *in vivo* for 2 weeks (Figure 5A). This novel *in vivo* test site in small animals was specifically chosen to impose a cyclic strain, through the mouse diaphragm contracting continuously with a respiratory rate of 80–230 bpm, on the transplanted rHTs. The imposed straining rate is comparable to the human fetal heart but without any electrical overdrive suppression of the hiPSC-PCMs by the host cells due to the lack of electrical coupling between the skeletal and cardiac myocytes.[33] Two weeks post-transplantation, strained-rSANHTs showed an upregulation of the pro-pacemaking transcription factors, *TBX3* (10.6-fold), *ISL1* (1.3-fold), and *SHOX2* (2.2-fold), and pacemaking *HCN1* (2.3-fold) and *HCN4* (2.3-fold) channels compared with the rLVHT control, albeit only *ISL1* and *TBX3* showed statistically significant changes ($p < 0.01$ in both cases; Figure 5B). There was no significant change in *cTNT*, *MLC2v*, *KCNA5,* or *TBX18* between the rHTs. *PITX2* expression was upregulated in the rSANHTs relative to the rLVHTs but did not reach statistical significance.

To assess the pacemaking protein expression in hiPSC-PCMs, whole-mount strained-rHTs were immunostained for protein of interest in conjunction with cTNT and quantified by image analysis. The $cTNT^+$ hiPSC-PCMs in the strained-rHTs maintained their self-organized clusters in the rSANHTs and the aligned bundles in the rLVHTs (Figures 5C–5F). The striated myofilaments were observed in both rHTs but were less ordered in the rSANHTs than the rLVHTs. Some hiPSC-PCMs from the transplanted rLVHTs had integrated into the host skeletal muscles, as indicated by the presence of $cTNT^+$ cells in the host diaphragm (Figure 5C). In contrast, fewer cells infiltrated the host skeletal muscle from the rSANHTs and the hiPSC-PCMs maintained a compact organization similar to the native SAN tissue. The origin of the $cTNT^+$ PCMs in the rHTs was confirmed by immunostaining with a human nuclear antigen antibody (Figure S6). Semi-quantifications showed that TBX18, TBX3, and HCN4 proteins were significantly upregulated by roughly 5.1-, 2.4-, and 18.4-fold, respectively, in the $cTNT^+$ cells in the rSANHTs compared with the rLVHTs (Figures 5C–5E). The inset, with a magnified view of the dashed line area in

the TBX18 image, clearly demonstrates that the nuclear expression of TBX18 is limited to the rSANHT graft and is not present in the surrounding host tissues. Connexins (CX)43, responsible for the electrical coupling between working CMs in the LV, exhibited 10-fold lower expression in hiPSC-PCMs in the rSANHTs compared with those in the rLVHTs (Figure 5F). Overall, our data suggest that in a mechanically active environment similar to the human heart, the SAN matrix preserves a pacemaker-like gene expression profile in the cyclic strained-hiPSC-PCMs, whereas those in the LV matrix are unable to maintain the pacemaking gene expression.

SAN ECM protects automaticity of hiPSC-PCMs from mechanical strain *in vivo*

To assess the electrophysiological function of the hiPSC-PCMs in the transplanted rHTs after 2 weeks of cyclic strain, we recorded CaTs of the strained-hiPSC-PCMs expressing GCaMP6f to indirectly evaluate the automaticity (Figure 6A). Paired rLVHTs —recellularized with the same batch of differentiated GCaMP6f-PCMs as the rSANHTs and engrafted on the contralateral diaphragm—were used as controls. Within 2 h of tissue extraction, 100% of the *in vivo* strained-rSANHTs (n = 6 of 6) generated spontaneous CaTs with a broad range of spontaneous firing rates (4–122 bpm). In contrast, only 33% of the strained-rLVHTs (n = 2 of 6) displayed spontaneous CaTs ($p = 0.014$ by χ^2 test; Figure 6B). Spontaneous CaTs were optically recorded using an epifluorescence microscope from each whole-mount rHT in the Tyrode's solution (Figure 6C; Videos S7 and S8). For rHTs without detectable CaTs, a multiphoton confocal microscope was used to confirm the absence of cyclic fluorescent signals. The frequency of spontaneous CaTs of hiPSC-PCMs in the strained-rLVHTs with automaticity was significantly slower than those in the strained-rSANHTs (median frequency: 37 vs. 61 bpm, $p < 0.001$ by Student's t test; Figure 6D), suggesting robust automaticity is preserved in hiPSC-PCMs recellularized in the SAN ECM after cyclic strain. The amplitude of the CaTs recorded from the strained-rSANHTs was significantly smaller than that from the rLVHTs (median $\Delta F/F_o$: 13 vs. 58%, $p = 0.005$ by Student's t test; Figure 6E; Table S2). An rLVHT with a slow frequency of automaticity could be captured by electrical pacing to exhibit 1:1 CaT to the stimulation frequency (Figure 6E). The presence of hiPSC-CMs was confirmed by immunostaining for cTNT in all strained-rLVHTs including those failed to generate spontaneous CaTs. Retention of drug sensitivity in the strained-rSANHTs after transplantation was demonstrated by the application of well-characterized drugs, isoproterenol and nifedipine, to elicit the response of a β-adrenoceptor agonist and a calcium channel blocker, respectively, in the rSANHTs. We observed a 20% increase in CaT frequency and an 80% increase in the normalized amplitude ($\Delta F/F_0$) upon the administration of 500 nM isoproterenol (Figure 6G), which is in agreement with the property of isoproterenol as a positive chronotrope and inotrope. Administration of 100 nM nifedipine induced a negative inotropic effect, as indicated by the complete cessation of CaTs (Figure 6H; Video S9). Our data demonstrated that only the SAN ECM, not the LV ECM, is able to retain the pacemaking function in the resident hiPSC-PCMs in a cyclic straining environment.

DISCUSSION

The limitations of electronic pacemakers have sparked interest in hiPSC-based biopacemakers as a potential alternative.[10] Current approaches have focused on the optimization of PCMs from hiPSCs by improving the differentiation efficiency and consequently the yield of functional PCMs.[10–14] Although improving the differentiation of hiPSC-PCMs is a critical first step for engineering a biopacemaker, the microenvironment that shapes the resident CM phenotype by providing the mechanical support and appropriate mechanotransduction in the resident cells may be equally critical in maintaining automaticity in the PCMs. Considering that the native ECM should be most supportive of its resident cells, we had extensively characterized the properties of the SAN ECM by examining the ultrastructure using scanning electron microscopy, the stiffness by atomic force microscopy, the biochemical composition by mass spectrometry, and the ECM protein spatial distribution relative to the resident CMs by immunostaining, which demonstrated distinct biochemical and biomechanical differences compared with that of the LV.[25] The SAN ECM is composed of >95% tensile-bearing collagens that surrounds the resident CMs compared with 74% in the LV. This is reflected in the 3-fold higher Young's modulus and the denser and more abundant fibrillar collagen network in the decellularized SAN than the LV ECM. Based on the ECM protein distribution in the tissues, the SAN ECM exhibits a composite material-like organization with regions of high elastin spanning between the stiffer collagen network that immediately surrounds the PCM clusters, whereas there is minimal protective tensile-bearing collagen around the working CMs and minimal elastin interspersed between the working CM bundles (Figure 7A). Based on this composite organization, we hypothesized that under active strain, the hiPSC-PCMs residing in the protective enclosure of the stiff, tensile-bearing collagen in the endomysial space would experience less strain as the collagen aids in resisting the strain, while the elastic perimysial region would undergo deformation to dissipate the strain (Figure 7B). This is in contrast to the LV ECM that does not provide the resident CMs with the same protective mechanisms, resulting in greater imposed strain on the working CMs. In this study, we directly tested this notion by determining the ability of the SAN ECM in promoting and preserving the pacemaking phenotype in the hiPSC-PCMs under cyclic strain by constructing the rSANHTs that are directly compared with rLVHTs.

SAN ECMs induce hiPSC-PCMs to form SAN-like cellular organization and morphology

Self-organization is a hallmark in cardiac development—a process that is instructed by complex yet tightly regulated signaling events—in which ECMs play an essential role.[34] In our study, the rSANHTs exhibited structural organization and cellular morphology that mimic the native SAN tissue and PCMs, respectively. Self-organization of hiPSC-PCMs in the rSANHTs is likely induced by (1) the ECM proteins serving as ligands with affinity for specific integrin isoforms expressed in the hiPSC-CMs and (2) the physical cues from the matrix geometry. Indeed, recellularization of whole hearts had reported endothelial cells homing to the inner lining of the blood vessels and hiPSC-CMs to the matrix scaffold region where the ventricular CMs had resided.[35] Thus, following the blueprint presented by the ECMs, hiPSC-CMs may preferentially bind and conform to the matrix regions where the native CMs had previously resided and not to residential regions of the fibroblasts, resulting

in the observed cellular organizational and morphological differences in the rHTs. The presence of islands of PCMs in the rSANHTs is consistent with our recent publication that reported PCM clusters surrounded by fibroblast clusters in the porcine SAN.[36] The minimal cell spreading with a lack of preferential alignment in the hiPSC-PCMs recellularized in the SAN ECMs but a clear alignment of the same cells in the LV ECMs, as indicated by the cellular aspect ratio and angle of alignment, is consistent with studies demonstrating regulation of hiPSC-CM morphology by patterned substrates.[37,38] The findings support the use of native ECMs as a blueprint in directing recellularized cells to organize and exhibit morphology of the native tissues.

SAN ECMs promote pacemaking phenotype and function in hiPSC-PCMs

Beyond cellular organization and morphology, the SAN ECMs promoted a pro-pacemaking gene profile in the recellularized hiPSC-PCMs, as demonstrated by both the transcript analysis by qPCR and protein expression from immunostaining of the rSANHTs compared with those in the rLVHTs. Functional data on contractility and CaTs also indicate the pacemaking phenotype of hiPSC-PCMs is better maintained by the SAN ECMs. Mechanistically, the SAN ECMs may modulate the gene expression and the current source-sink balance between the resident cell types.

First, the gene expression in hiPSC-PCMs can be modulated by the chemical and mechanical cues of the microenvironment. Indeed, *HCN4,* a pacemaking channel responsible for automaticity by driving the membrane clock of pacemaking function,[39] is upregulated in the rSANHTs. Transcription factors, *TBX3* and *TBX18*, known to inhibit the atrial CM phenotype and promote the PCM phenotype of the SAN head, respectively,[40,41] are also higher in the hiPSC-PCMs of the rSANHTs than the control. Hence, upregulation of these pacemaking genes likely contributes to the robust automaticity in hiPSC-PCMs recellularized in the SAN ECMs. Using mass spectrometry, we had previously reported >3-fold higher fibrillar collagens but >3-fold lower basement membrane-associated glycoproteins and non-fibrillar collagens in the SAN ECM relative to the LV ECM[25] Consequently, the integrin isoform-to-ligand binding pairs are likely different between the hiPSC-CMs residing in the rSANHTs and rLVHTs, activating distinct mechanotransduction pathways, resulting in differential cellular phenotypes. Indeed, differential phosphorylation of CX43 in atrial and ventricular tissues has been shown to be regulated by the specific integrin isoform that binds to the ECM ligand.[42] The SAN ECM that is stiffer compared with the LV ECM may also affect the mechanotransduction signaling and modulate the gene expression through the nuclear translocation of transcription co-regulators and the chromatin state.[43] In the rSANHTs, the abundant fibrillar collagens may be responsible for the clustering of the hiPSC-PCMs. This cell clustering, in contrast to a spread-out morphology in the rLVHTs, may lead to less cell-ECM contact and fewer engaged integrins. This agrees with the reported PCM-like electrophysiology with a fast frequency of automaticity in β1 integrin-deficient embryonic stem cell-derived CMs.[44]

Second, the cellular organization in the rSANHTs, dictated by the ECM blueprint, may affect the automaticity through the current source-sink balance between the PCMs and non-PCMs that results from their cluster organization. PCMs are the current source for

initiating spontaneous APs. Non-pacemaking cells, such as fibroblasts and working CMs, can act as a sink that draws current from the source, leading to suppressed automaticity in the PCMs to which they are electrically coupled.[45] Bressan et al. reported that collagen III is essential for the proper development of a functional SAN in the chick embryo by maintaining the proper cell-cell electrical coupling.[46] Therefore, in contrast to the LV ECM, the porcine SAN ECM blueprint with a higher abundance of fibrillar collagens I and III in the perimysium[25] could direct the cell density and cell type organization (the ratio of PCM to non-PCM clusters) to establish an optimal source-sink balance that is conducive for automaticity.

SAN ECMs protect automaticity of hiPSC-PCMs from *in vivo* cyclic strain

Working CMs in the LV mature and acquire increased cell size and an abundance of aligned myofilaments as a result of rising longitudinal strain due to hemodynamic load during cardiac development.[47,48] Accordingly, mechanical stretch mimicking the physiological environment of the heart has been employed as a strategy to mature working hiPSC-CMs by promoting cellular hypertrophy, alignment, organization, and functional properties of the adult contractile CMs, including the expression of ion channels and gap junctions.[31,32,49,50] However, a concurrent loss of automaticity, that is initially innate in all immature CMs, in the maturing neonatal LV CMs[51] suggests repeated mechanical stretch could negatively affect the PCM phenotype and function. Moreover, the lack of hypertrophy and myofilament development in PCMs in the SAN suggests that the PCMs may be protected from mechanical strain. We proposed a model on the protective mechanisms of the SAN ECM that may be responsible for reducing the strain experienced by the resident PCMs under cyclic contractions (Figure 7). Indeed, in agreement with our proposed model, the hiPSC-PCMs in the strained-rSANHTs remained self-organized similar to the native SAN with robust PCM gene expression and function. The high pacemaking gene expression in the rSANHTs (i.e., *HCN4*, *TBX3,* and *TBX18*), but more importantly the corresponding downregulation in the rLVHTs (i.e., *HCN4* and *TBX3*), supports the role of the SAN ECM in sustaining the pacemaking phenotype in hiPSC-PCMs under *in vivo* cyclic strain (Figure 7B).

Our rigorous experimental design, with the LV ECMs serving as the control, demonstrates that the pacemaking phenotype and gene expression in hiPSC-PCMs cannot be retained solely by any cardiac-derived ECM but specifically the SAN ECM. We theorize that the composite material-like organization in the SAN ECM with elastin fibers interspersed between PCM clusters would undergo mechanical deformation instead of the PCMs that are mechanically insulated in the stiff collagen matrix enclosure to minimize mechanotransduction signaling from stretch in the PCMs (Figure 7B). The preserved pacemaking function in the rSANHT and the lack of progression to a mature working CM phenotype, which typically coincides with an increase in postnatal mechanical stress,[48] may be attributed to a reduced mechanical strain in the hiPSC-PCMs seeded in the SAN ECM. This notion is also consistent with the retention of pacemaking function in adult rabbit PCMs *in vitro* with inhibited mechanofeedback from contractions.[52] Additionally, cyclic stretch has been shown to upregulate *CX43* in neonatal rat CMs and human embryonic stem cell-derived CMs.[53,54] Therefore, the low CX43 expression in the rSANHTs compared

with the rLVHTs indicates the PCMs in the rSANHTs may be experiencing a reduced mechanical strain in contrast to those in the rLVHTs. Collectively, the data support our proposed model that the SAN ECM, through its composite nature, may be preserving the pacemaking function in hiPSC-PCMs by shielding the cells from cyclic strain (Figure 7).

In summary, the current study provides new insights into the protective nature of the composite SAN ECM and presents a novel strategy for subjecting human cell-based biopacemaker under cyclic strain in small animals without electrical overdrive suppression. This study highlights the importance of the SAN matrix scaffold, not just any cardiac ECM, in retaining the PCM properties of the hiPSC-PCMs subjected to a cardiac-like cyclic strain. Hence, shielding the cyclic mechanical strain imposed on the PCMs should be included as a consideration in the design of the engineered biopacemakers. While we have reported the unique biochemical and biophysical properties of the SAN ECM,[25,36] the discrete factors in the matrix scaffold and the precise signaling pathways that are responsible for preserving the pacemaking function in hiPSC-PCMs under cyclic strain warrant further study.

Limitations of the study

One major limitation in this study is the use of a mixture of CM subtypes in recellularizing the ECMs. Although our PCM differentiation protocol increased the PCM fraction by up to 3-fold compared with the established CM differentiation protocol, the PCMs are still only ~30% of the total CMs. With future improvement in cardiac subtype differentiation, the resulting rSANHT could exhibit an even faster frequency of automaticity without the presence of working CMs that may be present as a current sink and depressing the pacemaking function. Additionally, the loss of automaticity in the engineered LV tissue constructs could be due to the maturation of the working CMs on the LV ECM. This, however, still supports our hypothesis that the SAN ECM promotes and preserves the pacemaking phenotype, whereas the LV ECM supports the contractile phenotype. One other limitation in the study is the use of Ca^{2+} transient recordings as surrogate for APs, rather than a direct AP measurement due to the difficulty of detecting the low fluorescence intensity of voltage-sensitive ArcLight against a high background autofluorescence stemming from collagen in the ECMs. The electrophysiological assessment could be improved as new brighter genetically encoded voltage-sensitive indicators become available.

STAR★METHODS

RESOURCE AVAILABILITY

Lead contact—Additional information and requests for resources and reagents should be directed to the lead corresponding author, Deborah K. Lieu, at dklieu@ucdavis.edu.

Materials availability—Additional information and requests for materials should be directed to the Lead Contact.

Data and code availability

- ed information of some experimental procedures is available online in Supplemental Information. Source data for Figures 1 to 6 and Figures S3

and S4 are included in Data S1. Additional data can be requested from the corresponding author.

- Our custom software used for quantifying CaTs is available online (https://amlab.shinyapps.io/spikemap/).
- Any additional information required to reanalyze the data reported in this work paper is available from the lead contact upon request.

EXPERIMENTAL MODEL AND SUBJECT DETAILS

hiPSC culture and differentiation to PCMs—HiPSC line, iPS-DF6–9-9T.B (WiCell), was cultured in StemMACS iPS-Brew XF (Miltenyi Biotec) in dishes coated with hESC-Qualified Matrigel (Corning) at 37°C with 5% CO_2 and subsequently differentiated into PCMs as previously described.[11] Briefly, confluent hiPSCs were differentiated in RPMI 1640 media supplemented with B-27 supplement minus insulin (ThermoFisher Scientific, 11875119 and A1895601) from days 0–7. To promote cardiogenesis, RPMI media was supplemented with 6 μM GSK3 inhibitor CHIR99021 (Tocris) from differentiation days 0–2 and with 5 μM WNT inhibitor IWR1 (Tocris) from differentiation days 3–5. Small molecule Nodal inhibitor SB431542 (Tocris) was added at days 3–5 to differentiate PCMs (Figure 1A). After D7 post-differentiation, hiPSC-CMs were maintained in RPMI 1640 media supplement with B-27 supplement with insulin (ThermoFisher Scientific, 17504044). Differentiated hiPSC-PCM culture were characterized by flow cytometry for CM yield by cTNT, immunostained for cTNT and pacemaking HCN4 channel, and classified into CM subtypes by optically recorded APs of isolated single cells by FluoVolt. hiPSC-PCMs were used to recellularize the porcine ECM scaffolds to test the role ECM in PCM phenotype and function.

Mice—NOD-SCID IL-2Rγ^{null} (NSG, The Jackson laboratory, IMSR_JAX:005557) mice ~12-week of age were used as bioreactors for *in vivo* cyclic strain testing of our rHTs. All animal usage and care followed the protocol approved by the Institutional Animal Care and Use Committee (IACUC) of the University of California, Davis and adhered to the guidelines of the National Institutes of Health.

METHOD DETAILS

Isolation and decellularization of porcine SAN and LV—Porcine hearts were chosen for their translational value given their similar physiology and ECM composition as that of human[56] to minimize species-mismatch and the precedence of FDA-approved porcine small intestine submucosa scaffold for clinical use. Fresh hearts of 6-month-old market hogs were obtained from the UC Davis Meat Laboratory. As previously described,[25] the SAN region was identified and manually dissected under a microscope (Figures S1A and S1B) and verified by trichrome staining (Figure S1C) and immunostaining for HCN4 channels to identify the pacemaking CMs (Figure S1D). For all experiments, the LV tissues dissected with consistent myocardial alignment served as the control. Tissues of 300-μm thick slices were decellularized to obtain SAN and LV matrix scaffolds as previously described[25] (Figure S2).

Fabrication of rSANHTs and rLVHTs with hiPSC-PCMs—To generate rSANHTs and rLVHTs, decellularized SAN and LV ECMs were each spread out in a well of a 24-well plate and dried to enable attachment to the culture surface. Prior to recellularization, ECMs were rehydrated overnight at 37°C in CM culture medium. HiPSC-PCMs of day 7–12 post-differentiation were seeded on a SAN or an LV ECM at 2.6×10^6 cells/cm^2. Cultured rHTs were assessed 14 days post-construction for phenotype and function as described below.

Cyclic mechanical strain rHTs *in vivo*—Heterotopic transplantation has been shown to allow vascularization of tissue constructs within two weeks and survival for at least 6 months,[57] suggesting the feasibility of utilizing the NSG mice as bioreactors for long-term *in vivo* testing of our rHTs. To impose cyclic mechanical strain at a frequency comparable to the human fetal heart rate (110–160 beats/min), the rHTs were heterotopically transplanted onto the thoracic diaphragm (80–230 breaths/min) of ~12-week-old NSG mice. No electrical overdrive suppression of the human PCMs by the host diaphragm is expected because CMs do not electrically couple with skeletal myocytes.[33] Each pair of rSANHT and rLVHT 2–3 days post-fabrication were transplanted contralaterally onto the diaphragm from an abdominal access for side-by-side comparison, with the cell-seeded side facing the diaphragm. Fibrin gel was used to secure the rHTs at the transplantation site. Engrafted rHTs were harvested 2 weeks after transplantation and analyzed for cardiac and pacemaker markers through immunostaining (Table S3) and transcription analysis (Table S4), or for functional assessment by calcium transient (CaT) recording as described for *in vitro* rHTs.

Assessment of gene expression and morphometry of hiPSC-PCMs in rSANHTs and rLVHTs—Transcript expression of rSANHTs for pacemaker genes of interest were analyzed by quantitative real-time PCR (Table S4) using SYBR Green that was normalized by GAPDH with rLVHTs as control using a ΔΔCT method. Protein expression of rHTs were assessed by whole-mount immunostaining for pacemaker and CM genes. Stained images were also analyzed for cell morphometric parameters, including area, major axis, and minor axis, by ImageJ to determine the aspect ratio and level of cellular elongation. The angle of alignment of CMs to myofibril in radian was plotted in MATLAB using a custom script.[55]

Contractile assessment of rSANHT and rLVHT—Contractile function of the regional PCMs in rSANHT or rLVHT attached to a dish and whole rHTs in suspension were measured optically at 37°C with 5% CO_2 in an on-stage incubator using an Observer Z1 microscope (Zeiss) at 10× magnification with an EMCCD camera (Photometrics). Spontaneous contractions of regional cells or clusters was quantified using the MUSCLEMOTION software.[27] The contractions were analyzed for frequency, peak amplitude, time-to-peak, and relaxation time. Contraction parameters of PCMs were averaged from 8 rSANHTs and 10 rLVHTs. Whole rHT contraction parameters were averaged from 20 rSANHTs and 16 rLVHTs. Representative maximum displacements of the rHTs were quantified by PIV analysis using MATLAB (MathWorks) with a custom MATLAB code based on MatPIV1.6.1.[55]

Functional assessment of automaticity—To assess automaticity of hiPSC-PCMs in rSANHTs and rLVhTs, GCaMP6f-hiPSC line expressing a genetically encoded calcium-sensitive indicator, GCaMP6f, driven by a constitutive CAG promoter and inserted at the AAVS1 locus was generated by CRISPR (manuscript in preparation) similarly as described in our publication for a voltage-sensitive hiPSC line,[58] allowing direct and repeated measurements of intracellular CaTs by avoiding possible issues associated with uneven fluorescent probe loading in thick rHTs.[59] CaTs were used as a surrogate for APs to assess automaticity since the fluorescence level of voltage-sensitive ArcLight-hiPSC-PCMs did not allow consistent and reliable measurement in the presence of a high autofluorescence from the ECMs and the spontaneous CaT frequency is equivalent to the frequency of automaticity.[60] Recordings of CaTs of rSANHT or rLVHT in Tyrode's solution at 37°C with 5% CO_2 were acquired using the GFP filter set at a sampling rate of ~100 fps using an Observer Z1 microscope (Zeiss) at 10× magnification with an EMCCD QuantEM:512SC camera (Photometrics) that is controlled by the Ocular 2.0 software. In some of the experiments, electric stimulation was applied with biphasic 4 ms pulses of 24 V/cm and 2 Hz using a C-Pace EM (IonOptix). Raw data and traces were then analyzed using our previously described R scripts[61] implemented as web application using R package "shiny".[62]

QUANTIFICATION AND STATISTICAL ANALYSIS

Summarized data in the results are presented as mean ± standard error of the mean (SEM) or median for non-normally distributed data. Datasets in boxplots are displayed as median with the interquartile range (Q1, Q3). Unless otherwise stated, indicated sample sizes (n) represent biological replicates as either individual heart tissues or individual recordings from four *in vitro* or two *in vivo* batches of experiments. For single-cell data, sample size (n) represents the number of cells analyzed from at least three independent experiments. Student's t-test (two-tailed) was performed for two-group or one-way ANOVA followed by Bonferroni post hoc test for multi-group (>2) comparisons, with $p < 0.05$ considered as statistically significant.

Supplementary Material

Refer to Web version on PubMed Central for supplementary material.

ACKNOWLEDGMENTS

This work is supported by grants from the California Institute for Regenerative Medicine (CIRM DISC2-10120 and DISC2-12663) and the National Institutes of Health (NIH R01HL159492) to D.K.L. C.W.C. is supported by the National Institutes of Health T32 Training Fellowship (T32HL086350). H.K.J.K. is supported by the CIRM Cell and Gene Therapy Training Fellowship (EDUC4-12792) to J.A.N. P.N.T. is supported by Harold S. Geneen Charitable Trust Awards Program for Coronary Heart Disease. S.O., A.B., and R.G. are supported by the CIRM Bridges to Stem Cells Training Fellowship (EDUC2-08390). B.A.C. is supported by the CIRM Bridges to Stem Cells Training Fellowship (EDUC2-12620). J.W.C. is funded by a National Science Foundation grant (NSF 1264776). N.C. is funded by NIH grants (R01HL085727, R01HL085844, and R01HL137228) and VA Merit Review Grants (I01BX 000576 and I01CX001490) as a part-time staff physician at VA Northern California Health Care System and is the holder of the Roger Tatarian Endowed Professorship in Cardiovascular Medicine.

INCLUSION AND DIVERSITY

We support inclusive, diverse, and equitable conduct of research.

REFERENCES

1. Boyett MR, Honjo H, and Kodama I (2000). The sinoatrial node, a heterogeneous pacemaker structure. Cardiovasc. Res. 47, 658–687. [PubMed: 10974216]
2. Lewis T (1910). Galvanometric curves yielded by cardiac beats generated in various areas of the auricular musculature: The pacemaker of the heart. Heart 24.
3. Uygur A, and Lee RT (2016). Mechanisms of Cardiac Regeneration. Dev. Cell 36, 362–374. [PubMed: 26906733]
4. Writing Group Members; Mozaffarian D, Benjamin EJ, Go AS, Arnett DK, Blaha MJ, Cushman M, Das SR, de Ferranti S, Després JP, et al. (2016). Heart Disease and Stroke Statistics-2016 Update: A Report From the American Heart Association. Circulation 133, e38–e360. [PubMed: 26673558]
5. Tung RT, Shen WK, Hayes DL, Hammill SC, Bailey KR, and Gersh BJ (1994). Long-term survival after permanent pacemaker implantation for sick sinus syndrome. Am. J. Cardiol. 74, 1016–1020. [PubMed: 7977039]
6. Adán V, and Crown LA (2003). Diagnosis and treatment of sick sinus syndrome. Am. Fam. Physician 67, 1725–1732. [PubMed: 12725451]
7. Li RA (2012). Gene- and cell-based bio-artificial pacemaker: what basic and translational lessons have we learned? Gene Ther. 19, 588–595. [PubMed: 22673497]
8. Maisel WH (2006). Pacemaker and ICD generator reliability: meta-analysis of device registries. JAMA 295, 1929–1934. [PubMed: 16639052]
9. Rosen MR, Brink PR, Cohen IS, and Robinson RB (2004). Genes, stem cells and biological pacemakers. Cardiovasc. Res. 64, 12–23. [PubMed: 15364609]
10. Protze SI, Liu J, Nussinovitch U, Ohana L, Backx PH, Gepstein L, and Keller GM (2017). Sinoatrial node cardiomyocytes derived from human pluripotent cells function as a biological pacemaker. Nat. Biotechnol. 35, 56–68. [PubMed: 27941801]
11. Yechikov S, Kao HKJ, Chang CW, Pretto D, Zhang XD, Sun YH, Smithers R, Sirish P, Nolta JA, Chan JW, et al. (2020). NODAL inhibition promotes differentiation of pacemaker-like cardiomyocytes from human induced pluripotent stem cells. Stem Cell Res. 49, 102043. [PubMed: 33128951]
12. Liang W, Han P, Kim EH, Mak J, Zhang R, Torrente AG, Goldhaber JI, Marbán E, and Cho HC (2020). Canonical Wnt signaling promotes pacemaker cell specification of cardiac mesodermal cells derived from mouse and human embryonic stem cells. Stem Cell. 38, 352–368.
13. Ren J, Han P, Ma X, Farah EN, Bloomekatz J, Zeng XXI, Zhang R, Swim MM, Witty AD, Knight HG, et al. (2019). Canonical Wnt5b Signaling Directs Outlying Nkx2.5+ Mesoderm into Pacemaker Cardiomyocytes. Dev. Cell 50, 729–743.e5. [PubMed: 31402282]
14. Liu F, Fang Y, Hou X, Yan Y, Xiao H, Zuo D, Wen J, Wang L, Zhou Z, Dang X, et al. (2020). Enrichment differentiation of human induced pluripotent stem cells into sinoatrial node-like cells by combined modulation of BMP, FGF, and RA signaling pathways. Stem Cell Res. Ther. 11, 284. [PubMed: 32678003]
15. Porzionato A, Stocco E, Barbon S, Grandi F, Macchi V, and De Caro R (2018). Tissue-Engineered Grafts from Human Decellularized Extracellular Matrices: A Systematic Review and Future Perspectives. Int. J. Mol. Sci. 19, 4117. [PubMed: 30567407]
16. Taylor DA, Chandler AM, Gobin AS, and Sampaio LC (2017). Maximizing Cardiac Repair: Should We Focus on the Cells or on the Matrix? Circ. Res. 120, 30–32. [PubMed: 28057787]
17. Mirsadraee S, Wilcox HE, Korossis SA, Kearney JN, Watterson KG, Fisher J, and Ingham E (2006). Development and characterization of an acellular human pericardial matrix for tissue engineering. Tissue Eng. 12, 763–773. [PubMed: 16674290]

18. Mirsadraee S, Wilcox HE, Watterson KG, Kearney JN, Hunt J, Fisher J, and Ingham E (2007). Biocompatibility of acellular human pericardium. J. Surg. Res. 143, 407–414. [PubMed: 17574597]

19. Moroni F, and Mirabella T (2014). Decellularized matrices for cardiovascular tissue engineering. Am. J. Stem Cells 3, 1–20. [PubMed: 24660110]

20. Oberwallner B, Brodarac A, Choi YH, Saric T, Anić P, Morawietz L, and Stamm C (2014). Preparation of cardiac extracellular matrix scaffolds by decellularization of human myocardium. J. Biomed. Mater. Res. 102, 3263–3272.

21. Sánchez PL, Fernández-Santos ME, Costanza S, Climent AM, Moscoso I, Gonzalez-Nicolas MA, Sanz-Ruiz R, Rodríguez H, Kren SM, Garrido G, et al. (2015). Acellular human heart matrix: A critical step toward whole heart grafts. Biomaterials 61, 279–289. [PubMed: 26005766]

22. Guyette JP, Charest JM, Mills RW, Jank BJ, Moser PT, Gilpin SE, Gershlak JR, Okamoto T, Gonzalez G, Milan DJ, et al. (2016). Bioengineering Human Myocardium on Native Extracellular Matrix. Circ. Res. 118, 56–72. [PubMed: 26503464]

23. Johnson TD, Hill RC, Dzieciatkowska M, Nigam V, Behfar A, Christman KL, and Hansen KC (2016). Quantification of decellularized human myocardial matrix: A comparison of six patients. Proteonomics Clin. Appl. 10, 75–83.

24. Kappler B, Anic P, Becker M, Bader A, Klose K, Klein O, Oberwallner B, Choi YH, Falk V, and Stamm C (2016). The cytoprotective capacity of processed human cardiac extracellular matrix. J. Mater. Sci. Mater. Med. 27, 120. [PubMed: 27272902]

25. Gluck JM, Herren AW, Yechikov S, Kao HKJ, Khan A, Phinney BS, Chiamvimonvat N, Chan JW, and Lieu DK (2017). Biochemical and biomechanical properties of the pacemaking sinoatrial node extracellular matrix are distinct from contractile left ventricular matrix. PLoS One 12, e0185125. [PubMed: 28934329]

26. Lian X, Hsiao C, Wilson G, Zhu K, Hazeltine LB, Azarin SM, Raval KK, Zhang J, Kamp TJ, and Palecek SP (2012). Robust cardiomyocyte differentiation from human pluripotent stem cells via temporal modulation of canonical Wnt signaling. Proc. Natl. Acad. Sci. USA 109, E1848–E1857. [PubMed: 22645348]

27. Sala L, van Meer BJ, Tertoolen LGJ, Bakkers J, Bellin M, Davis RP, Denning C, Dieben MAE, Eschenhagen T, Giacomelli E, et al. (2018). MUSCLEMOTION: A Versatile Open Software Tool to Quantify Cardiomyocyte and Cardiac Muscle Contraction In Vitro and In Vivo. Circ. Res. 122, e5–e16. [PubMed: 29282212]

28. Sun YH, Sun Y, Zhu K, Reid B, Gao X, Draper BW, Zhao M, and Mogilner A (2018). Electric fields accelerate cell polarization and bypass myosin action in motility initiation. J. Cell. Physiol. 233, 2378–2385. [PubMed: 28749047]

29. Tseng Q, Duchemin-Pelletier E, Deshiere A, Balland M, Guillou H, Filhol O, and Théry M (2012). Spatial organization of the extracellular matrix regulates cell-cell junction positioning. P Natl Acad Sci USA 109, 1506–1511.

30. Broussard GJ, Liang Y, Fridman M, Unger EK, Meng G, Xiao X, Ji N, Petreanu L, and Tian L (2018). In vivo measurement of afferent activity with axon-specific calcium imaging. Nat. Neurosci. 21, 1272–1280. [PubMed: 30127424]

31. Yang X, Pabon L, and Murry CE (2014). Engineering adolescence: maturation of human pluripotent stem cell-derived cardiomyocytes. Circ. Res. 114, 511–523. [PubMed: 24481842]

32. Gu X, Zhou F, and Mu J (2021). Recent Advances in Maturation of Pluripotent Stem Cell-Derived Cardiomyocytes Promoted by Mechanical Stretch. Med. Sci. Mon. Int. Med. J. Exp. Clin. Res. 27, e931063.

33. Reinecke H, MacDonald GH, Hauschka SD, and Murry CE (2000). Electromechanical coupling between skeletal and cardiac muscle. Implications for infarct repair. J. Cell Biol. 149, 731–740. [PubMed: 10791985]

34. Hofbauer P, Jahnel SM, Papai N, Giesshammer M, Deyett A, Schmidt C, Penc M, Tavernini K, Grdseloff N, Meledeth C, et al. (2021). Cardioids reveal self-organizing principles of human cardiogenesis. Cell 184, 3299–3317.e22. [PubMed: 34019794]

35. Hochman-Mendez C, Mesquita FCP, Morrissey J, da Costa EC, Hulsmann J, Tang-Quan K, Xi Y, Lee PF, Sampaio LC, and Taylor DA (2022). Restoring anatomical complexity of a left

ventricle wall as a step toward bioengineering a human heart with human induced pluripotent stem cell-derived cardiac cells. Acta Biomater. 141, 48–58. [PubMed: 34936938]

36. Smithers RL, Kao HKJ, Zeigler S, Yechikov S, Nolta JA, Chan JW, Chiamvimonvat N, and Lieu DK (2021). Making Heads or Tails of the Large Mammalian Sinoatrial Node Micro-Organization. Circ. Arrhythm. Electrophysiol. 14, e010465.
37. Shum AMY, Che H, Wong AOT, Zhang C, Wu H, Chan CWY, Costa K, Khine M, Kong CW, and Li RA (2017). A Micropatterned Human Pluripotent Stem Cell-Based Ventricular Cardiac Anisotropic Sheet for Visualizing Drug-Induced Arrhythmogenicity. Adv. Mater. 29.
38. Wang J, Chen A, Lieu DK, Karakikes I, Chen G, Keung W, Chan CW, Hajjar RJ, Costa KD, Khine M, and Li RA (2013). Effect of engineered anisotropy on the susceptibility of human pluripotent stem cell-derived ventricular cardiomyocytes to arrhythmias. Biomaterials 34, 8878–8886. [PubMed: 23942210]
39. Honjo H, Boyett MR, Kodama I, and Toyama J (1996). Correlation between electrical activity and the size of rabbit sino-atrial node cells. J. Physiol. 496, 795–808. [PubMed: 8930845]
40. Wiese C, Grieskamp T, Airik R, Mommersteeg MTM, Gardiwal A, de Gier-de Vries C, Schuster-Gossler K, Moorman AFM, Kispert A, and Christoffels VM (2009). Formation of the sinus node head and differentiation of sinus node myocardium are independently regulated by Tbx18 and Tbx3. Circ. Res. 104, 388–397. [PubMed: 19096026]
41. Hoogaars WMH, Engel A, Brons JF, Verkerk AO, de Lange FJ, Wong LYE, Bakker ML, Clout DE, Wakker V, Barnett P, et al. (2007). Tbx3 controls the sinoatrial node gene program and imposes pacemaker function on the atria. Genes Dev. 21, 1098–1112. [PubMed: 17473172]
42. Boateng SY, Lateef SS, Mosley W, Hartman TJ, Hanley L, and Russell B (2005). RGD and YIGSR synthetic peptides facilitate cellular adhesion identical to that of laminin and fibronectin but alter the physiology of neonatal cardiac myocytes. Am. J. Physiol. Cell Physiol. 288, C30–C38. [PubMed: 15371257]
43. Miroshnikova YA, Nava MM, and Wickström SA (2017). Emerging roles of mechanical forces in chromatin regulation. J. Cell Sci. 130, 2243–2250. [PubMed: 28646093]
44. Fässler R, Rohwedel J, Maltsev V, Bloch W, Lentini S, Guan K, Gullberg D, Hescheler J, Addicks K, and Wobus AM (1996). Differentiation and integrity of cardiac muscle cells are impaired in the absence of beta 1 integrin. J. Cell Sci. 109, 2989–2999. [PubMed: 9004034]
45. Fahrenbach JP, Mejia-Alvarez R, and Banach K (2007). The relevance of non-excitable cells for cardiac pacemaker function. J. Physiol. 585, 565–578. [PubMed: 17932143]
46. Bressan M, Henley T, Louie JD, Liu G, Christodoulou D, Bai X, Taylor J, Seidman CE, Seidman JG, and Mikawa T (2018). Dynamic Cellular Integration Drives Functional Assembly of the Heart's Pacemaker Complex. Cell Rep. 23, 2283–2291. [PubMed: 29791840]
47. Patey O, Carvalho JS, and Thilaganathan B (2019). Perinatal changes in cardiac geometry and function in growth-restricted fetuses at term. Ultrasound Obstet. Gynecol. 53, 655–662. [PubMed: 30084123]
48. Bernardo BC, Weeks KL, Pretorius L, and McMullen JR (2010). Molecular distinction between physiological and pathological cardiac hypertrophy: experimental findings and therapeutic strategies. Pharmacol. Ther. 128, 191–227. [PubMed: 20438756]
49. Földes G, Mioulane M, Wright JS, Liu AQ, Novak P, Merkely B, Gorelik J, Schneider MD, Ali NN, and Harding SE (2011). Modulation of human embryonic stem cell-derived cardiomyocyte growth: a testbed for studying human cardiac hypertrophy? J. Mol. Cell. Cardiol. 50, 367–376. [PubMed: 21047517]
50. Ovchinnikova E, Hoes M, Ustyantsev K, Bomer N, de Jong TV, van der Mei H, Berezikov E, and van der Meer P (2018). Modeling Human Cardiac Hypertrophy in Stem Cell-Derived Cardiomyocytes. Stem Cell Rep. 10, 794–807.
51. Cerbai E, Pino R, Sartiani L, and Mugelli A (1999). Influence of postnatal-development on I(f) occurrence and properties in neonatal rat ventricular myocytes. Cardiovasc. Res. 42, 416–423. [PubMed: 10533577]
52. Segal S, Kirschner Peretz N, Arbel-Ganon L, Liang J, Li L, Marbach D, Yang D, Wang SQ, and Yaniv Y (2019). Eliminating contraction during culture maintains global and local Ca(2+) dynamics in cultured rabbit pacemaker cells. Cell Calcium 78, 35–47. [PubMed: 30594820]

53. Salameh A, Wustmann A, Karl S, Blanke K, Apel D, Rojas-Gomez D, Franke H, Mohr FW, Janousek J, and Dhein S (2010). Cyclic mechanical stretch induces cardiomyocyte orientation and polarization of the gap junction protein connexin43. Circ. Res. 106, 1592–1602. [PubMed: 20378856]
54. Shen N, Knopf A, Westendorf C, Kraushaar U, Riedl J, Bauer H, Pöschel S, Layland SL, Holeiter M, Knolle S, et al. (2017). Steps toward Maturation of Embryonic Stem Cell-Derived Cardiomyocytes by Defined Physical Signals. Stem Cell Rep. 9, 122–135.
55. Zhang Y, Xu G, Lee RM, Zhu Z, Wu J, Liao S, Zhang G, Sun Y, Mogilner A, Losert W, et al. (2017). Collective cell migration has distinct directionality and speed dynamics. Cell. Mol. Life Sci. 74, 3841–3850. [PubMed: 28612218]
56. Johnson TD, Dequach JA, Gaetani R, Ungerleider J, Elhag D, Nigam V, Behfar A, and Christman KL (2014). Human versus porcine tissue sourcing for an injectable myocardial matrix hydrogel. Biomater. Sci. 2014.
57. Komae H, Sekine H, Dobashi I, Matsuura K, Ono M, Okano T, and Shimizu T (2017). Three-dimensional functional human myocardial tissues fabricated from induced pluripotent stem cells. J. Tissue Eng. Regen. Med. 11, 926–935. [PubMed: 25628251]
58. Sun YH, Kao HKJ, Chang CW, Merleev A, Overton JL, Pretto D, Yechikov S, Maverakis E, Chiamvimonvat N, Chan JW, and Lieu DK (2020). Human induced pluripotent stem cell line with genetically encoded fluorescent voltage indicator generated via CRISPR for action potential assessment post-cardiogenesis. Stem Cell. 38, 90–101.
59. Broyles CN, Robinson P, and Daniels MJ (2018). Fluorescent, Bioluminescent, and Optogenetic Approaches to Study Excitable Physiology in the Single Cardiomyocyte. Cells 7.
60. Shinnawi R, Huber I, Maizels L, Shaheen N, Gepstein A, Arbel G, Tijsen AJ, and Gepstein L (2015). Monitoring Human-Induced Pluripotent Stem Cell-Derived Cardiomyocytes with Genetically Encoded Calcium and Voltage Fluorescent Reporters. Stem Cell Rep. 5, 582–596.
61. Yechikov S, Copaciu R, Gluck JM, Deng W, Chiamvimonvat N, Chan JW, and Lieu DK (2016). Same-Single-Cell Analysis of Pacemaker-Specific Markers in Human Induced Pluripotent Stem Cell-Derived Cardiomyocyte Subtypes Classified by Electrophysiology. Stem Cell. 34, 2670–2680.
62. Winston Chang JC, Allaire JJ, Xie Y, and McPherson J (2018). Shiny: Web Application Framework for R. R Package.

Highlights

- Reconstructed sinoatrial node heart tissues (rSANHTs) with hiPSC-pacemaking cells in matrices
- rSANHT structural organization recapitulates features of the native SAN
- SAN extracellular matrix promotes pacemaking gene expression and functionality
- SAN extracellular matrix protects loss of automaticity in rSANHTs from *in vivo* cyclic strain

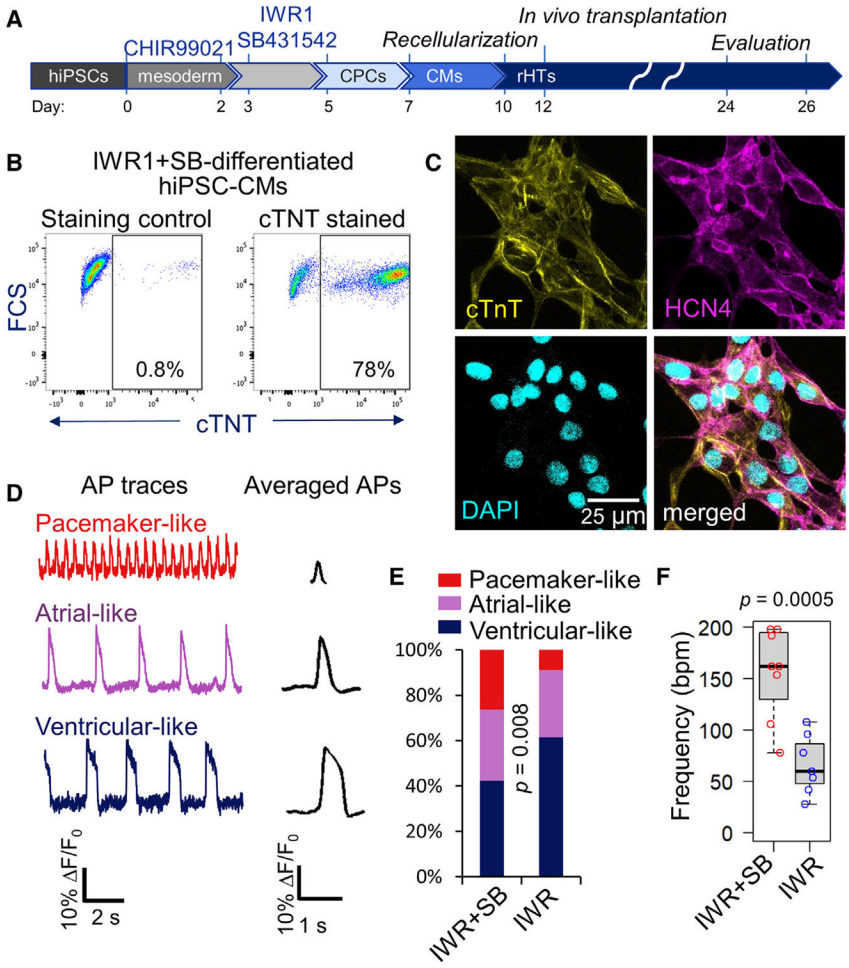

Figure 1. Differentiation and testing of hiPSC-PCMs

(A) Experimental timeline from cardiac differentiation, construction of rHTs by recellularization with hiPSC-PCMs, to *in vivo* transplantation and functional tests of rHTs.

(B) Representative flow cytometry dot plots of IWR1+SB-differentiated hiPSC-PCMs immunostained for cTNT vs. forward scatter (FCS) showing cardiomyogenesis efficiency of ~78% at day 20 post-differentiation. Dot plot for staining control with secondary antibody only is also shown.

(C) Representative confocal images showing hiPSC-CMs labeled for cTNT (yellow), HCN4 (magenta), and nuclear counterstain DAPI (cyan).

(D) Representative optical recordings and profiles of spontaneous APs of ventricular-, atrial- and pacemaker-like CMs.

(E) Population distribution of the hiPSC-CM subtypes ~60 days after differentiation with IWR1+SB (n = 256 cells) vs. IWR1 only (n = 63 cells) as classified by APs. p = 0.008 by χ^2 test.

(F) Spontaneous beating rates of the hiPSC-CM monolayers differentiated by IWR1+SB (n = 8) vs. IWR1 (n = 7). Data shown as median ± interquartile range. p = 0.0005 by Student's t test.

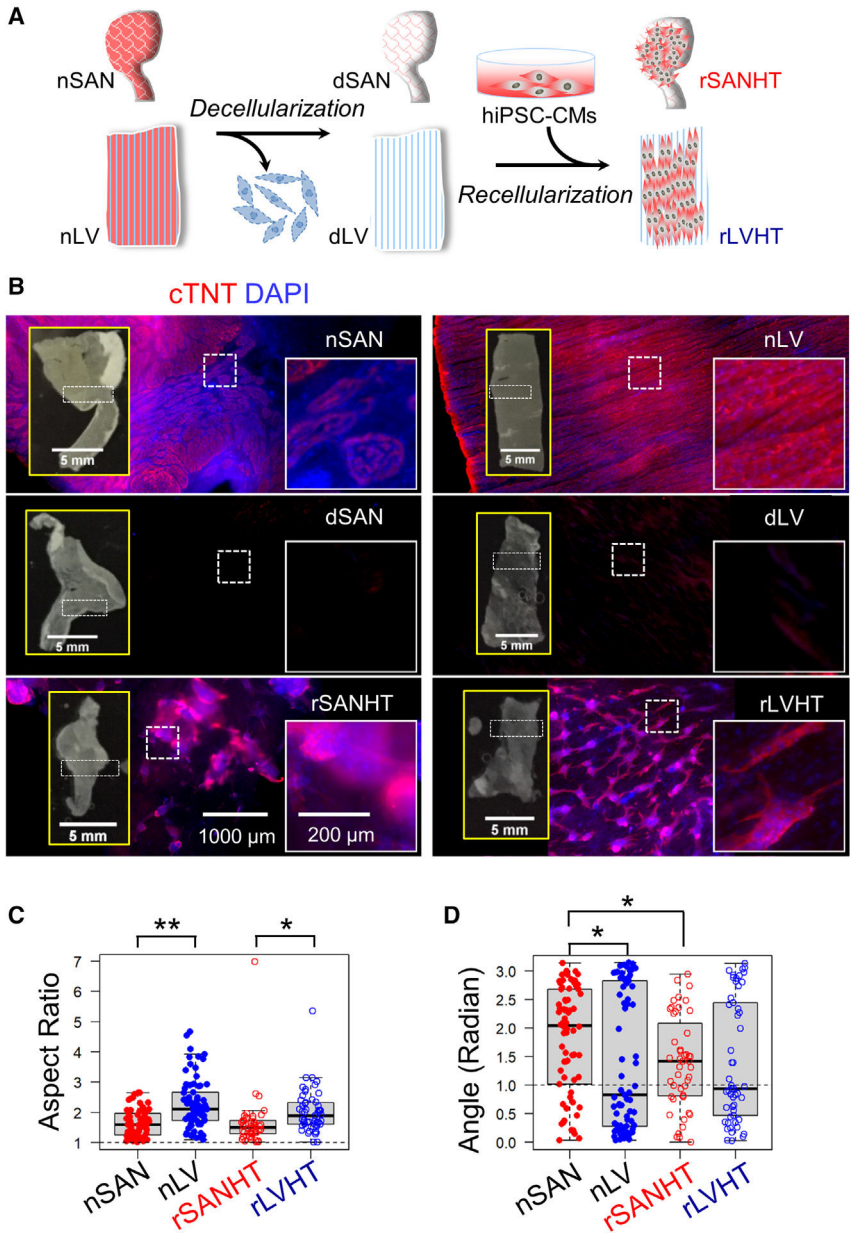

Figure 2. Generating rHTs that structurally mimic the native SAN and ventricular myocardium

(A) An illustration depicting the rHT construction processes.

(B) Representative images of whole-mount native (n) SAN, nLV, decellularized (d)SAN, dLV, rSANHTs and rLVHTs stained for cTNT and DAPI. Rectangular dashed outline in the bright-field tissue image indicates the location of the stitched fluorescence image shown. A magnified inset image is shown for the dashed square region in each stitched fluorescence image.

(C) Quantification of the aspect ratio for cell nuclei relative to the cell body in the native tissues and rHTs. *p <0.05, **p <0.01 by one-way ANOVA followed by Bonferroni post hoc test.

(D) Quantification of angle in radian (π) of nuclei relative to orientation of myofibrils in the native tissues or relative to orientation of the collagen fibers in recellularized SAN or LV ECMs (n = 3). All data in boxplots are shown as median ± interquartile range. *$p < 0.05$ by one-way ANOVA followed by Bonferroni post hoc test. (See Figure S3 for detailed morphometric quantification of the PCMs in native SAN relative to the adjacent atrial CMs.).

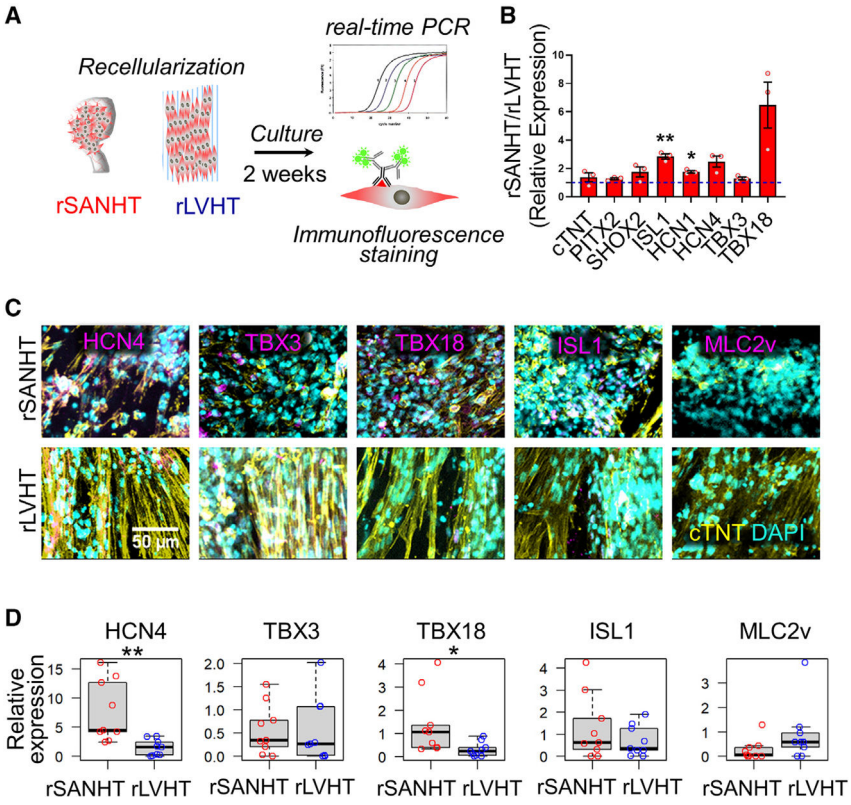

Figure 3. Pacemaker transcript and protein expression in the rSANHT and rLVHT

(A) An experimental schematic of gene expression analyses of rSANHTs and rLVHTs.

(B) Bar graph of relative pacemaking gene expression of rSANHT to rLVHT. Data are presented as the mean ± SEM of the relative fold changes of rSANHT to rLVHT (n = 3). *p < 0.05, **p < 0.01 by Student's t test.

(C) Representative fluorescence images showing immunostaining of pacemaking genes—HCN4, TBX3, TBX18 and ISI1—and ventricular-specific MLC2v in rSANHTs and rLVHTs (magenta). rHTs were co-stained with general CM marker cTNT (yellow) and nuclear counterstain DAPI (cyan).

(D) Quantification of relative protein expression of rSANHTs and rLVHTs for TBX18, TBX3, HCN4, ISL1, and CX43. Relative mean fluorescence intensities that colocalized either with the DAPI and cTNT (TBX18, TBX3, and ISL1) or with cTNT alone (HCN4 and CX43) were quantified from nine confocal images of three independent experiments (rSANHT: n = 3; rLVHT: n = 3). All data in boxplots are shown as median ± interquartile range. *p < 0.05, **p < 0.01 by Student's t test.

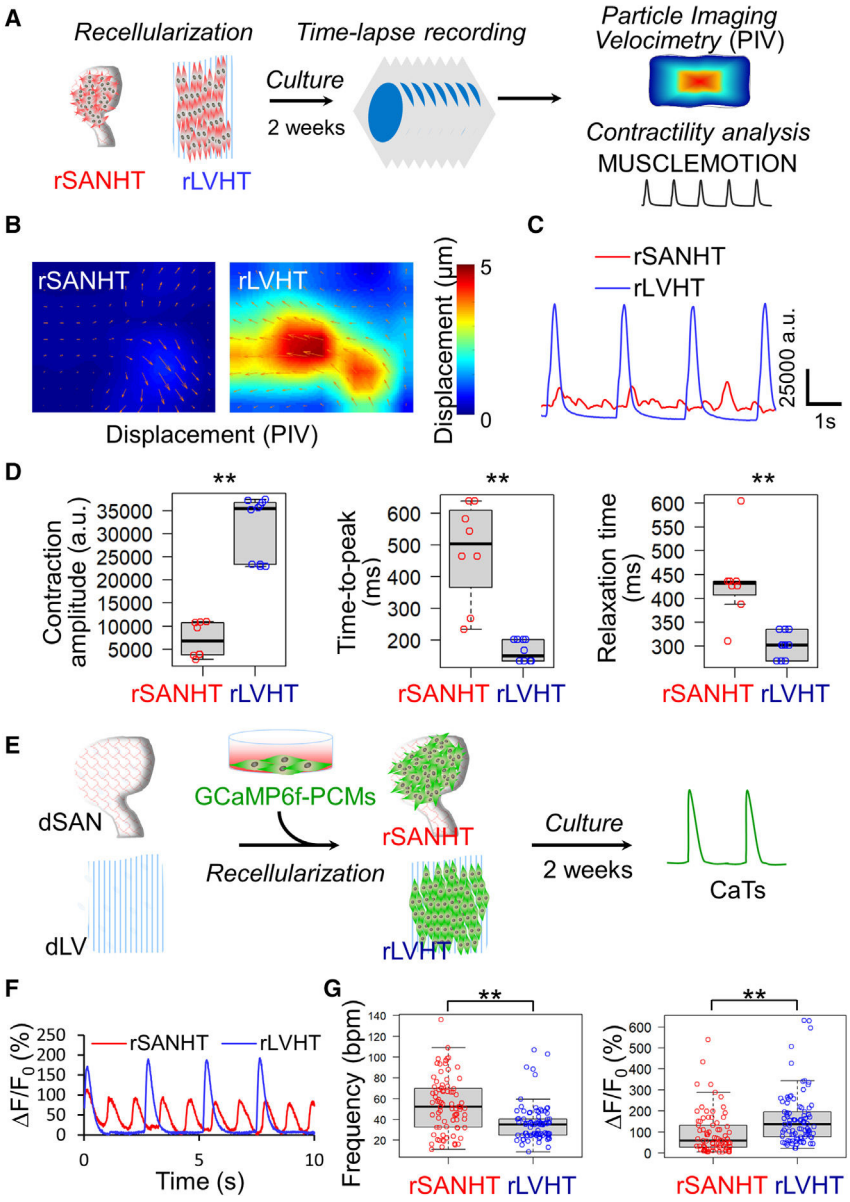

Figure 4. Functional assessment of the hiPSC-PCMs in the rSANHTs and rLVHTs

(A) A schematic overview of contractility analysis approaches in assessing regional contractions of hiPSC-PCMs in the rHTs 2 weeks after recellularization.

(B) Representative maximum displacements of rHTs calculated by particle imaging velocimetry (PIV) analysis.

(C) Representative contractile traces of the hiPSC-PCMs in rSANHTs and rLVHTs quantified by MUSCLEMOTION. Traces were normalized to arbitrary unit (a.u.).

(D) Quantification of contraction amplitude, time-to-peak, and relaxation time of the regional hiPSC-CMs in rSANHT (n = 8) and rLVHT (n = 10).

(E) A schematic overview of the experimental workflow for CaT assessment in rSANHTs and rLVHTs.

(F) Representative spontaneous CaT traces of the hiPSC-PCMs residing in an SAN or LV ECM after 2 weeks of recellularization.
(G) Quantification of spontaneous CaT frequency (bpm) and amplitude ($\Delta F/F_o$) of spontaneously generated CaTs for the hiPSC-PCMs in rSANHTs (n = 80 events) and rLVHTs (n = 91 events) from three independent experiments. All data in boxplots are shown as median ± interquartile range. **$p < 0.01$ by Student's t test.

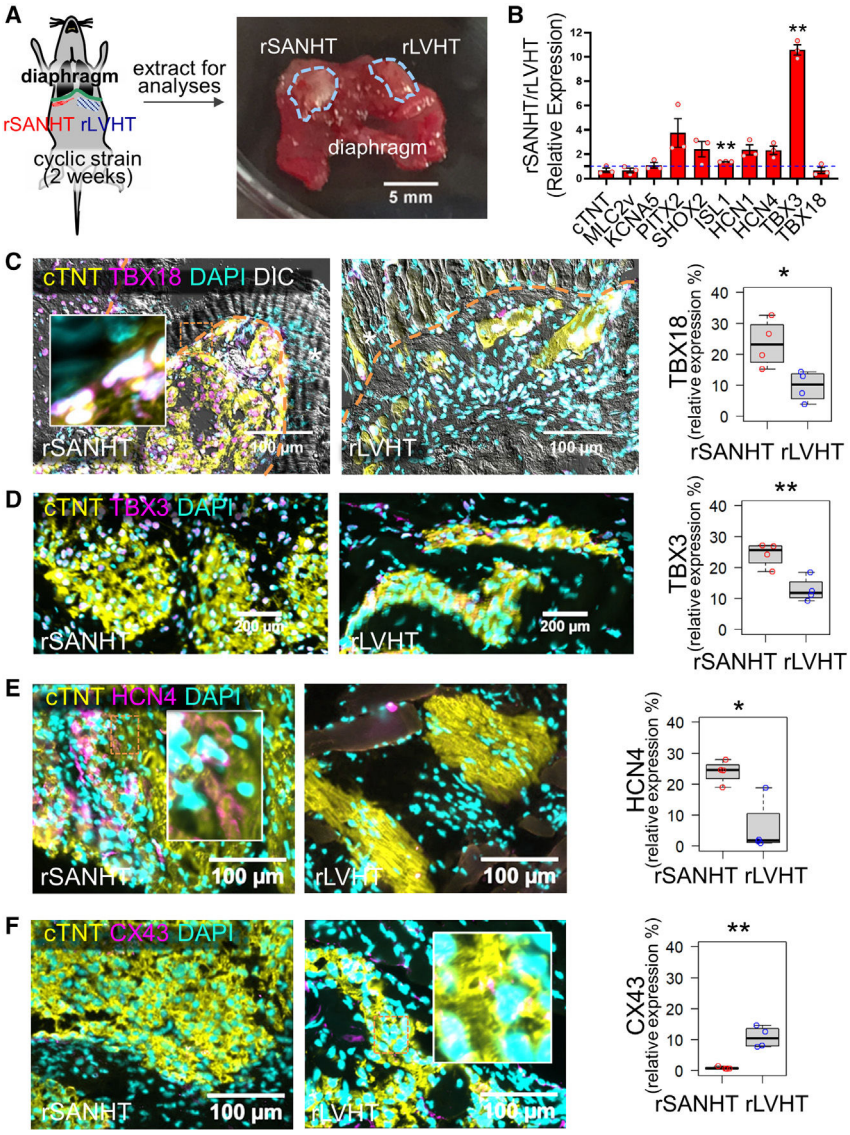

Figure 5. Phenotype of hiPSC-PCMs in cyclic strained-rSANHT and rLVHT

(A) A diagram of the experimental design for *in vivo* cyclic straining of rHTs and a representative gross morphology of extracted rSANHT and rLVHT transplanted on the thoracic diaphragm after cyclic mechanical strain of 2 weeks.

(B) Bar graph showing relative transcript expression of the rSANHTs to the rLVHTs after *in vivo* cyclic strain. Data are presented as mean relative fold changes with SEM of rSANHT vs. rLVHT with GAPDH normalization (n = 3). **p < 0.01 by Student's t test.

(C–F) Immunostaining and quantification of relative protein expression in cyclic strained-rSANHTs and rLVHTs for TBX18, TBX3, HCN4, and CX43 (magenta). Recovered transplants were co-stained with general CM marker cTNT (yellow) and nuclear counterstain DAPI (cyan). The orange dashed lines in (C) delineate the boundary between the grafted rHTs and host skeletal muscle tissues. White asterisks in the images indicate the host skeletal muscle tissues revealed by the differential interference contrast (DIC) overlay. Relative fluorescence intensities of protein expression were quantified from four confocal

images of two independent transplantation experiments (rSANHT: n = 3; rLVHT: n = 3). Magnified insets highlight each respective dashed rectangular region. All data in boxplots are shown as median ± interquartile range. *p < 0.05, **p < 0.01 by Student's t test.

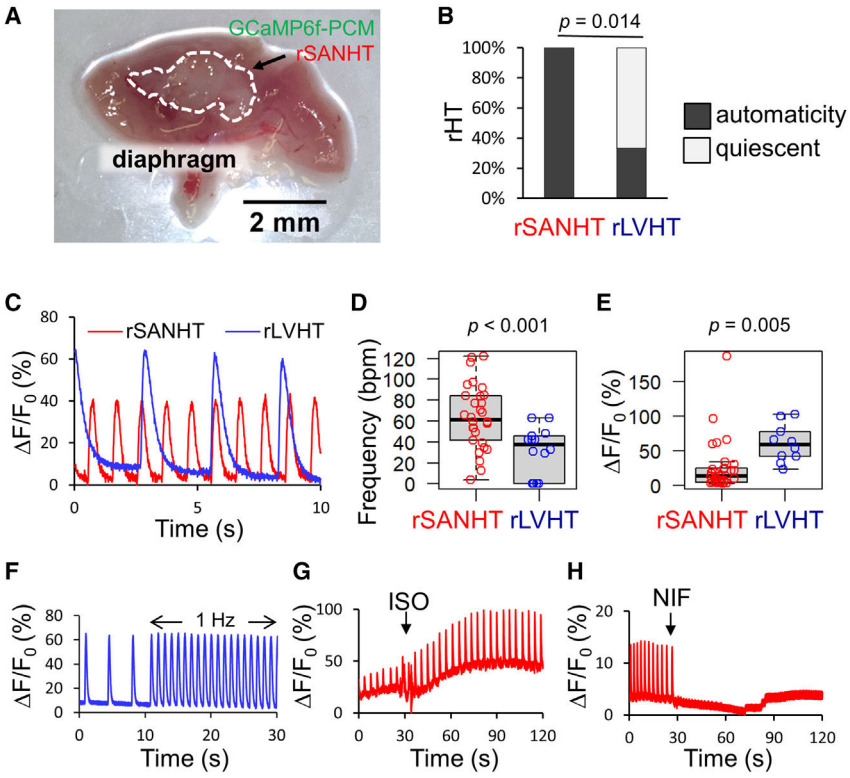

Figure 6. Automaticity and spontaneous CaTs of hiPSC-PCMs in cyclic strained-rSANHTs and rLVHTs

(A) Representative gross morphology of an rSANHT recellularized with GCaMP6f-PCMs transplanted on the thoracic diaphragm of NSG mice and subjected to cyclic mechanical strain for 2 weeks.

(B) Stacked bar graph showing 66% of *in vivo* strained-rLVHTs (four out of six mice) lost automaticity, while 100% of strained-rSANHTs (six out of six mice) maintained robust automaticity. p = 0.014 by χ^2 test.

(C) Representative spontaneous CaTs optically recorded from a rSANHT and a rLVHT graft extracted after cyclic strain.

(D) Quantification of spontaneous CaT frequency from rSANTHTs and rLVHTs. Data were pooled from two independent transplantations of six rSANHTs (n = 30 regions) and two spontaneously beating rLVHTs (n = 10 regions). For the other four not beating rLVHTs, we treat their bpm as 0 (n = 4). p < 0.001 by Student's t test.

(E) Quantification of spontaneous and baseline-normalized CaT amplitude ($\Delta F/F_0$) from rSANTHTs and rLVHTs. Data were pooled from two independent transplantations of six rSANHTs (n = 30 regions) and two rLVHTs (n = 10 regions). p = 0.005 by Student's t test. All data in boxplots are shown as median ± interquartile range.

(F) Optical recording of CaTs from an rLVHT graft under electrical pacing of 1 Hz.

(G) Representative CaTs of an rSANHT graft in response to 500 nM isoproterenol.

(H) Representative CaTs of a rSANHT graft in response to 100 nM nifedipine.

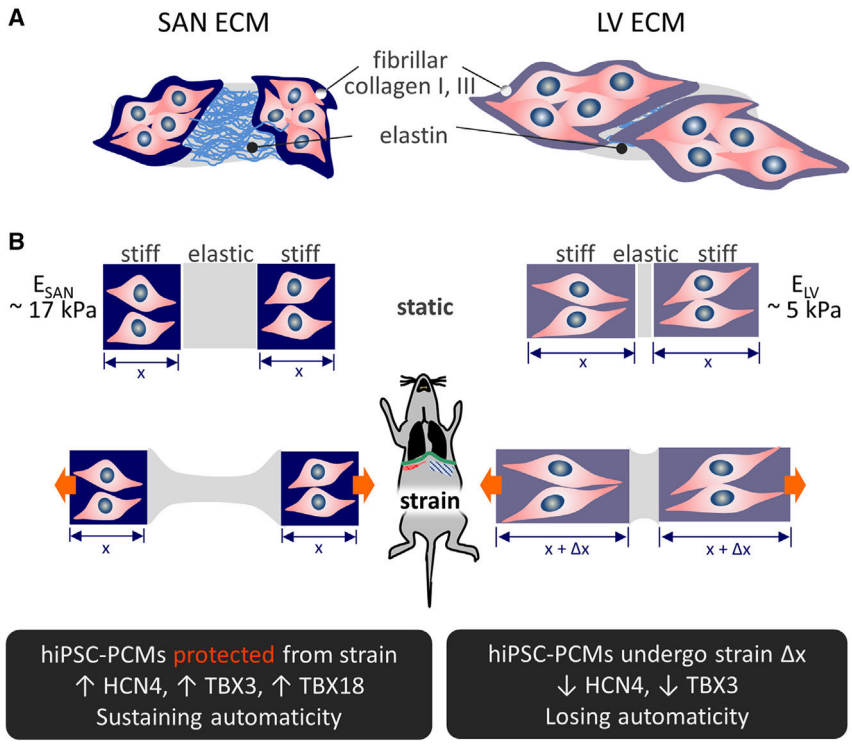

Figure 7. Model on the protective mechanisms of the SAN ECM under cyclic mechanical strain

(A) A diagram illustrating the ECM protein distribution that yields the composite nature of the SAN ECM compared with the LV ECM.

(B) A model describing the protective mechanisms of SAN ECM in preserving the pacemaking phenotype and function of the resident PCMs under cyclic strain compared with the LV counterpart.

KEY RESOURCES TABLE

REAGENT or RESOURCE	SOURCE	IDENTIFIER
Antibodies		
Mouse anti-cardiac troponin T IgG1	ThermoFisher Scientific	Cat# MA5–12960; RRID: AB_11000742
Mouse anti-cardiac troponin T IgG2a	Developmental Studies Hybridoma Bank (DSHB)	Cat# CT3; RRID: AB_528495
Mouse anti-TBX18 IgG2a	Sigma-Aldrich	Cat# SAB1412362
Rabbit anti-CX43 IgG	Abcam	Cat# ab11370; RRID: AB_297976
Rabbit anti-HCN4 IgG	Alomone Labs	Cat# APC-052; RRID: AB_2039906
Rabbit anti-TBX3 IgG	ThermoFisher Scientific	Cat# 42–4800; RRID: AB_2533526
Rabbit anti-MLC2v IgG	Proteintech	Cat# 10906–1-AP; RRID: AB_2147453
Wheat-germ agglutinin	ThermoFisher Scientific	Cat# W11261
Mouse anti-human nuclei (HuNu) IgG1	Sigma-Aldrich	Cat# MAB1281; RRID: AB_94090
Goat anti-Mouse IgG1 Alexa Fluor 488	ThermoFisher Scientific	Cat# A-21121; RRID: AB_2535764
Goat anti-Mouse IgG2a Alexa Fluor 488	ThermoFisher Scientific	Cat# A-21131; RRID: AB_2535771
Goat anti-Mouse IgG2b Alexa Fluor 488	ThermoFisher Scientific	Cat# A-21141; RRID: AB_2535778
Goat anti-Rabbit Alexa Fluor 488	ThermoFisher Scientific	Cat# A-11034; RRID: AB_2576217
Goat anti-Mouse IgG1 Alexa Fluor 546	ThermoFisher Scientific	Cat# A-21123; RRID: AB_2535765
Goat anti-Mouse IgG2a Alexa Fluor 546	ThermoFisher Scientific	Cat# A-21133; RRID: AB_2535772
Goat anti-Mouse IgG1 Alexa Fluor 647	ThermoFisher Scientific	Cat# A-21240; RRID: AB_2535809
Goat anti-Mouse IgG2a Alexa Fluor 647	ThermoFisher Scientific	Cat# A-21241; RRID: AB_2535810
Goat anti-Rabbit Alexa Fluor 647	ThermoFisher Scientific	Cat# A-21245; RRID: AB_2535813
Biological samples		
Porcine hearts	UC Davis Meat Laboratory	N/A
Chemicals, peptides, and recombinant proteins		
Nifedipine	Sigma-Aldrich	Cat# N7634
Isoproterenol	Sigma-Aldrich	Cat# PHR2722
hESC-Qualified Matrigel	Corning	Cat# 354277
CHIR99021	Tocris	Cat# 4423
Y-27632	Tocris	Cat# 1253
IWR1	Tocris	Cat# 3532
SB431542	Tocris	Cat# 1614
DAPI	Vector Laboratories	Cat# H-1200–10
Hoechst 33342	ThermoFisher	Cat# 62249
FluoVolt	ThermoFisher	Cat# F10488
Critical commercial assays		
PureLink RNA Mini Kit	ThermoFisher	Cat# 12183018A
SYBR Green Master Mix	ThermoFisher	Cat# A46012

REAGENT or RESOURCE	SOURCE	IDENTIFIER
C-Pace EM	IonOptix	https://www.ionoptix.com/products/components/stimulators/c-pace-em/
Experimental models: Cell lines		
hiPSC	WiCell	Cat# ÍPS-DF6–9-9T.B
Experimental models: Organisms/strains		
NSG mice	The Jackson Laboratory	Strain # 005557
Oligonucleotides		
Primers	This paper	Table S4
Software and algorithms		
FlowJo	BD Biosciences	https://www.flowjo.com/
Prism	GraphPad	https://www.graphpad.com/scientific-software/prism/
ImageJ	NIH	https://ImageJ.nih.gov/ij/
MATLAB	MathWorks	https://www.mathworks.com/products/matlab.html
Ocular	Photometrics	https://www.photometrics.com/products/ocular
Spike mapping (v1.0)	Sun etal., 2019[55]	https://amlab.shinyapps.io/spikemap/
MUSCLEMOTION	Salaetal., 2018[27]	https://www.ahajournals.oro/doi/suppl/10.1161/CIRCRCIRCR.117.312067